J. Fluid Mech. (2011), *vol.* 674, *pp.* 43–66. © Cambridge University Press 2011
doi:10.1017/S0022112010006373

Thrust efficiency of harmonically oscillating flexible flat plates

PAULO J. S. A. FERREIRA DE SOUSA[1,2]† AND JAMES J. ALLEN[1]

[1]Department of Mechanical and Aerospace Engineering, New Mexico State University, Las Cruces, NM 88003, USA

[2]Department of Mechanical Engineering/LASEF, Instituto Superior Técnico, Avenue Rovisco Pais, 1, 1049-001 Lisboa, Portugal

(Received 18 August 2009; revised 16 October 2010; accepted 12 December 2010; first published online 2 March 2011)

We consider the efficiency of thrust-producing inextensible membranes with variable bending rigidities. The present study is a numerical investigation of the thrust generation and flow-field characteristics of a two-dimensional flapping flexible membrane, fixed at its leading edge. To study the time-dependent response of the membranes, a fluid/structure solver that couples a compact finite-difference immersed boundary method flow solver with a thin-membrane structural solver was developed. Using a body-fitted grid, external forcing to the structure is calculated from the boundary fluid dynamics. A systematic series of runs of the fluid/structure solver was performed in order to obtain a clear picture of the thrust-producing characteristics of membranes with bending rigidities ranging between $EI = 5 \times 10^{-6}$ and $EI = 2 \times 10^{-5}$ and structural mass coefficients between $\rho_s h = 0.01$ and $\rho_s h = 0.04$, for a Reynolds number of $Re = 851$.

Key words: flow–structure interactions, propulsion, swimming/flying

1. Introduction

Fish use predominant oscillatory movements in order to propel themselves. Gray (1933) noted that fish swimming movement could be mainly described as a combination of two wave-like phenomena. One is cyclic change of the curved shape of the body showing a lateral wave of curvature running in the caudal direction, and the other is every single point of the body performing, in consequence of the wave of lateral curvature on the body, a sinusoidal track in a horizontal plane. Thus, a flexible membrane problem is of interest parallel to the swimming fish, since the backbone motion of fish species is essentially similar to that of the travelling wave. Lighthill was the first to study the fluid dynamics of fish swimming with a theory for evaluating reactive forces between an undulating fish body and the water surrounding it (see Lighthill 1970, 1975). Before that, Wu (1961, 1971) had shed light on the inviscid hydrodynamics of fish-like propulsion.

More recent research has turned attention to fish and their aquatic counterparts for inspiration in designing compact and efficient autonomous and unmanned underwater

† Present address: Department of Mechanical Engineering, Vanderbilt University, Nashville, TN 37240, USA. Email address for correspondence: ferreiradesousa@gmail.com

https://doi.org/10.1017/S0022112010006373 Published online by Cambridge University Press

vehicles (e.g. Bandyopadhyay *et al.* 1997; Triantafyllou, Triantafyllou & Yue 2000; Anderson & Chabra 2002; Bandyopadhyay 2005). Historically, experimental studies on unsteady thrust production have focused on the use of an aerofoil in steady forward motion with a combination of harmonic heaving and pitching to produce thrust, see Koochesfahani (1989) and Anderson *et al.* (1998). The reason an aerofoil has been typically used for experimental studies is that it represents a reasonable approximation to the lunate tail of the larger groups of fish, classified as swimming in Caringiform mode, see Lighthill (1975). A foil in steady forward motion and a combination of harmonic heaving and pitching motions produces thrust through the formation of a flow downstream from the trailing edge, which when averaged over one period of oscillation has the form of a jet. The harmonic motion of the foil causes unsteady shedding of vorticity from the trailing edge, while there are also particular conditions that cause the formation of leading-edge vortices. The interaction between the unsteady vorticity shed by the foil and the wake dynamics which results in the formation of patterns of large-scale eddies has been shown through several visualizations, see for example Koochesfahani (1989). As would be expected, the number of vortices formed per half-cycle varies with the amplitude and frequency of the motion and the shape of the waveform (Koochesfahani 1989). When thrust is generated by an oscillating foil, the wake behind it has an average velocity profile with the form of a jet. This jet flow is associated with a staggered array of vortices moving downstream from the foil, closely resembling the von Kármán vortex street behind bluff objects, but with reverse rotational direction (Triantafyllou, Triantafyllou & Grosenbaugh 1993). Triantafyllou, Triantafyllou & Gopalkrishnan (1991) have shown that optimal creation of a jet occurs at non-dimensional frequencies corresponding to the maximum spatial growth of the unstable average jet flow behind the foil, and that the propulsive efficiency reaches a maximum under these conditions. Studies of the two-dimensional wake patterns behind flapping foils and live and robotic swimming fish have been performed both experimentally and numerically. Extensive reviews of this research can be found in the literature (Triantafyllou, Techet & Hover 2004; Triantafyllou *et al.* 2005). More recently, Schnipper, Andersen & Bohr (2009) experimentally investigated the wake structures produced by a symmetric foil performing pitching oscillations in a vertically flowing soap film. The frequency and amplitude of the oscillation were varied over a wide range, and the wake types were mapped out in a phase diagram spanned by the width-based Strouhal number and the dimensionless amplitude.

Buchholz & Smits (2006) visualized wakes produced by a rigid panel of aspect ratio $AR = 0.54$, pitching about its leading edge in a free stream at Reynolds number $Re_c = 640$. In Buchholz & Smits (2008), the thrust performance was investigated for the same configuration and using different aspect ratio panels. For $Re_c = O(10^4)$, thrust coefficient was found to depend primarily on Strouhal number St and the aspect ratio of the panel AR. Propulsive efficiency was sensitive to aspect ratio only for AR less than 0.83. Nevertheless, the magnitude of the peak efficiency of a given panel with variation in Strouhal number varied inversely with the amplitude to span ratio A/S, while the Strouhal number of optimum efficiency increased with increasing A/S. Peak efficiencies between 9 % and 21 % were measured.

Limited studies have been performed examining the effects of flexibility on unsteady thrust production. Jiménez *et al.* (2003) studied experimentally the wake structures issuing from flexible panels with an aspect ratio of $AR = 0.27$. The panels were actuated to approximate streamwise travelling waves, and it was shown that for the symmetry plane, a vortex was shed into the wake near the peak displacement of the

https://doi.org/10.1017/S0022112010006373 Published online by Cambridge University Press

trailing edge. Along with this vortex, another vortex was formed from the shedding of a shear layer as the trailing edge swept across the wake. This vortex formed a counter-rotating vortex pair with the following vortex shed in the subsequent half-cycle. Prempraneech, Hover & Traintafyllou (2003) utilized aerofoils of relatively high stiffness to investigate flexibility effects on efficiency and thrust production. Compared to the rigid foil control, flexible foils were found to be in general more efficient. It was also found that at Strouhal numbers greater than 0.30, aerofoil flexibility resulted in a decrease in the thrust coefficient relative to the stiff case. Work by Liao *et al.* (2003) pointed to practical propulsion applications of using harmonically driven pitching flexible membranes. This problem also has interest from a aero-elasticity point of view.

A flat plate is the simplest aerofoil. It is simple to build and a propulsion system based on a flat plate, either rigid or flexible, would be extremely attractive for engineering applications. A flat plate pitching at the leading edge, while not necessarily the most efficient flapping propulsive device, is the simplest in terms of geometry and lends itself well to comparison with inviscid theory and simple iteration of the effects of foil stiffness. Early analytical work on two-dimensional waving plates as a model for the swimming of fish was performed by Wu (1961). By fully deriving the potential flow field as a result of a prescribed motion, Wu (1961) was able to make predictions about efficiency and thrust as a function of the nature of the kinematic motion of the plate. A key result was that the thrust is higher for plates with longer wavelengths and the trend was for efficiency to increase as the wavelength of the plate decreases. This implies that the rate of decrease in thrust is slower than the rate of decrease in power as the wavelength decreases. This result has important consequences for the current study as the oscillation wavelength of the flexible plate is obviously shorter than the rigid one. Wu (1961) showed that the thrust coefficient of the rigid plate is higher than the travelling wave, while the efficiency of the travelling wave case is higher than the rigid case. In Allen & Smits (2001), a simplified description of the motion of a flexible membrane was obtained by fitting the experimental data with solutions of the Euler–Bernoulli beam equation. It was shown that the modal contributions start to decay significantly past mode 4 and hence the motion of the flexible membrane can be described by a fairly compact data set.

In the present paper, we consider the two-dimensional flexible membrane problem in an unbounded fluid domain. The effects of structural mass coefficient and bending rigidity on the system propulsion ability are examined. To examine the full nonlinear problem, we developed a coupled fluid–structure method of the Navier–Stokes equations and geometrically nonlinear structural equations. We purposely limited the present work to a one degree-of-freedom pitching pattern in order to limit the number of free parameters and focus on the fundamental effect of solid mass coefficient and rigidity on the thrust performance.

2. Problem statement

We consider the problem of a thin membrane that is clamped at the leading edge and free on the trailing edge. The pitching angle at the leading edge is harmonically oscillated and interacts with a uniform incompressible viscous free-stream flow U_∞ in an unbounded domain, as shown in figure 1. The membrane is considered to be sufficiently thin such that its thickness and variation with length do not have an impact on the results. The structural properties of the membrane in this two-dimensional study are the length L, mass per length ρ_s and bending rigidity EI, where E is Young's modulus and I the second moment of inertia.

https://doi.org/10.1017/S0022112010006373 Published online by Cambridge University Press

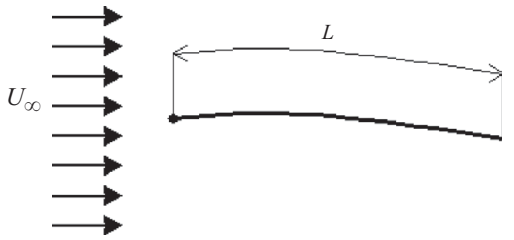

FIGURE 1. Depiction of the problem of the harmonically oscillating flexible flat plate with length L in a uniform free-stream flow U_∞. The membrane is clamped at the leading edge and free on the trailing edge.

The equation of motion for a two-dimensional membrane is (Connell & Yue 2007)

$$\rho_s h \frac{\partial^2 \boldsymbol{x}}{\partial t^2} - \frac{\partial}{\partial s}\left(T(s)\frac{\partial \boldsymbol{x}}{\partial s}\right) + EI\frac{\partial^4 \boldsymbol{x}}{\partial s^4} = \boldsymbol{F}, \tag{2.1}$$

where s is the Lagrangian coordinate along the length of the membrane, $\boldsymbol{x}$ is the body position vector fixed at the leading edge, ρ_s is the structural density, h is the membrane thickness, $T(s)$ is the tension in the body, and EI is the structural bending rigidity. Fluid coupling comes through the forcing term defined as

$$\boldsymbol{F} = [\Delta\boldsymbol{\tau}]\boldsymbol{n}, \tag{2.2}$$

where $\boldsymbol{n}$ is the upward-pointing normal and $[\Delta\boldsymbol{\tau}]$ is the difference between the fluid-dynamic stress tensor at the top and bottom of the body.

The fluid dynamics are obtained as the solution to the incompressible fluid momentum and mass conservation equations, the Navier–Stokes equations, written as

$$\frac{\partial \boldsymbol{u}}{\partial t} + (\boldsymbol{u}\cdot\nabla)\boldsymbol{u} = \nu\nabla^2\boldsymbol{u} - \nabla p + \boldsymbol{f}, \tag{2.3}$$

$$\nabla\cdot\boldsymbol{u} = 0. \tag{2.4}$$

The influence of the membrane motion is effected on the fluid through the boundary condition given by

$$v = \frac{\partial x}{\partial t} \tag{2.5}$$

on the membrane boundary.

3. Fluid/structure coupled numerical model

We developed a coupled fluid–structure method to study the coupled nonlinear problem of flapping aero-elastic structures. The fluid-dynamic solver is a finite-difference solution to the Navier–Stokes equations solved with an immersed boundary method using a body-fitted auxiliary grid. Fluid-dynamic forcing on the body surface is calculated and used as input to a finite-difference structural-dynamic solver. The structural solver is geometrically nonlinear and able to take on arbitrary configurations. Both solvers are explicit and use a Runge–Kutta fourth-order time-discretization scheme.

https://doi.org/10.1017/S0022112010006373 Published online by Cambridge University Press

3.1. *Immersed boundary fluid solver*

The unsteady incompressible form of the continuity and Navier–Stokes equations for a Newtonian fluid was considered:

$$\nabla \cdot \boldsymbol{u} = 0, \tag{3.1}$$

$$\frac{\partial \boldsymbol{u}}{\partial t} + (\boldsymbol{u} \cdot \nabla)\boldsymbol{u} = \nu \nabla^2 \boldsymbol{u} - \nabla p, \tag{3.2}$$

where $\boldsymbol{u}$ is the fluid velocity, p is the pressure divided by density, and ν is the kinematic viscosity of the fluid. The momentum equations are spatially discretized on a staggered mesh by finite differences and all derivatives are evaluated with implicit fourth-order compact finite difference schemes. The fourth-order-accurate Runge–Kutta scheme was used for temporal discretization. In the developed two-dimensional (2-D) immersed boundary method, an implementation of the forcing of Mohd-Yusof (1997) was used in order to implement the immersed boundary. The immersed boundary flow solver is described in detail by Ferreira de Sousa, Pereira & Allen (2009).

3.1.1. *Validation and verification of the immersed boundary fluid solver*

Validation of the method will be performed through comparison with experimental results from Dickinson & Götz (1993). The reference experimental results considered two-dimensional starting flow about a flat plate of length L. The transition from rest to a fixed translational velocity of $0.1\,\mathrm{m\,s^{-1}}$ was done by a constant acceleration of $0.625\,\mathrm{m\,s^{-2}}$, which for a kinematic viscosity of $2.6 \times 10^{-5}\,\mathrm{m^2\,s^{-1}}$ gives a Reynolds number of $Re = 192$. It is shown that for this experiment, the forces on the flat plate reach a steady state after they have travelled seven chord lengths for angles of attack lower than 13.5°. These results were compared with steady-state results obtained by the present method. The computational domain considered spans over $0 < x, y < 0.80\,\mathrm{m}$ and the chord length is $c = 0.2\,\mathrm{m}$. A grid with 401^2 nodes was used and the time step was set to $\Delta t = 0.001\,\mathrm{s}$. To be consistent with the conventional definition of lift and drag in aerofoil theory, the forces are decomposed into drag, C_D, anti-parallel to the flow at infinity, and lift, C_L, orthogonal to the flow at infinity.

Comparisons with experimental results of Dickinson & Götz (1993) for the force coefficients after two chord lengths are presented in figure 2. Direct plots of the force coefficients against angle of attack are shown for angles of attack smaller than or equal to 9°, which is an appropriate comparison in the context of the present study. Force coefficients for this configuration encompassing a full range of angles of attack were earlier reported by Ferreira de Sousa *et al.* (2009). Figure 2(*a*) shows the comparison between the results obtained with the present method and the reference experimental results for C_L. The data for C_L are also compared to the predictions of thin aerofoil theory. The overall agreement between the two data sets is very good. As expected, the present method predicts higher lift coefficients for the lower angles of attack, more in line with thin aerofoil theory. Figure 2(*b*) shows the comparison for the drag coefficient C_D. Again, the agreement with experimental results is good, with the present method being capable of capturing the trend of the variation of the drag coefficient with angle of attack.

Verification of the method was performed via systematic grid convergence testing in Ferreira de Sousa *et al.* (2009). Comparing results of the present method for the L_2 norm with the grid convergence results for Fadlun *et al.* (2000) and Zhang & Zheng (2007) showed that the present method represents a clear improvement, with

https://doi.org/10.1017/S0022112010006373 Published online by Cambridge University Press

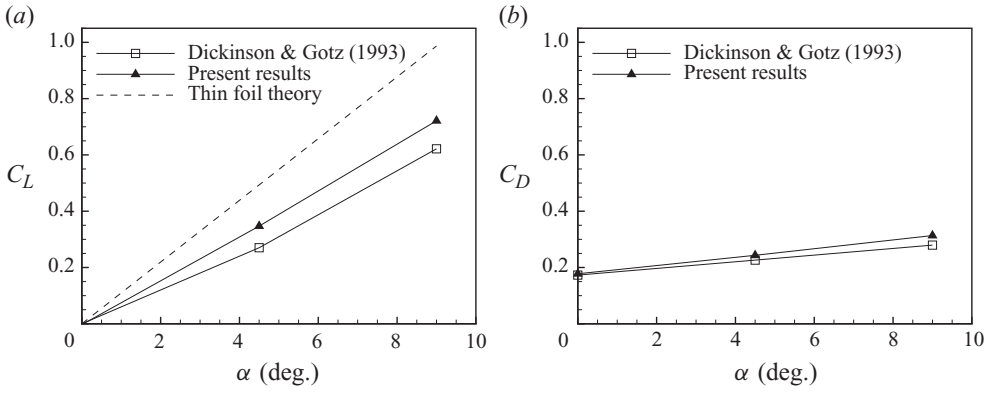

FIGURE 2. Comparison with experimental results of (*a*) the lift and (*b*) drag coefficients for angles of attack smaller than 10°. Results after two chord lengths.

the convergence of the L_2 norm being significantly better than second-order. Note that the grid convergence results provide only one way to determine the approximate order of accuracy of the current immersed boundary method, and we are not trying to resolve the issue of convergence of immersed boundary-like methods. The overall convergence issue involving interface jumps, like those encountered in the present method, was studied by Tornberg & Engquist (2004). The fact that the maximum error converges with a first-order slope obviously affects the results for the global norm L_2. Therefore, even if the formal order of accuracy for the finite difference schemes is fourth-order, that is not completely recovered in the global results because of the maximum error first-order convergence. This is the reason why the method achieves approximately third-order accuracy for the L_2 norm. It should be noted that even if these error convergence results are lower than the formal order of accuracy for the finite difference schemes used in the spatial discretization of the momentum equations, the verified order of accuracy for the present method is significantly better than the second-order accurate methods (that necessarily have first-order convergence for the L_∞ norm as well, Tornberg & Engquist 2004).

3.2. *Structural solver*

A finite-difference structural solver is developed, which allows for arbitrary orientation and configuration of the membrane. The equations of motion are derived in Cartesian coordinates and are equivalent to those used for the structural component by Zhu & Peskin (2002) and Connell & Yue (2007), permitting arbitrary configuration and orientation of the body:

$$\rho_s h \frac{\partial^2 \boldsymbol{x}}{\partial t^2} - Eh \frac{\partial}{\partial s}\left(\left(1 - \left(\frac{\partial \boldsymbol{x}}{\partial s}\cdot\frac{\partial \boldsymbol{x}}{\partial s}\right)^{-1/2}\right)\frac{\partial \boldsymbol{x}}{\partial s}\right) + EI\frac{\partial^4 \boldsymbol{x}}{\partial s^4} = \boldsymbol{F} \tag{3.3}$$

with boundary conditions

$$\boldsymbol{x} = 0, \quad \frac{\partial \boldsymbol{x}}{\partial s} = f(t) \quad \text{for } s = 0, \tag{3.4}$$

$$-Eh\left(1 - \left(\frac{\partial \boldsymbol{x}}{\partial s}\cdot\frac{\partial \boldsymbol{x}}{\partial s}\right)^{-1/2}\right)\frac{\partial \boldsymbol{x}}{\partial s} + EI\frac{\partial^3 \boldsymbol{x}}{\partial s^3} = 0, \quad \frac{\partial^2 \boldsymbol{x}}{\partial s^2} = 0 \quad \text{for } s = L, \tag{3.5}$$

https://doi.org/10.1017/S0022112010006373 Published online by Cambridge University Press

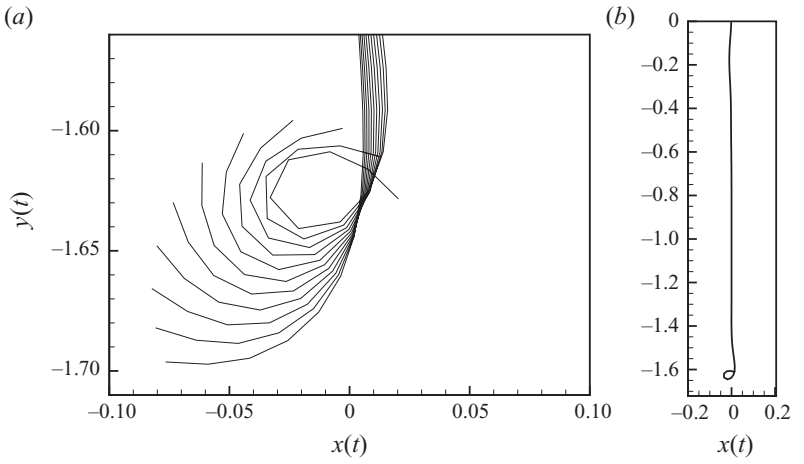

FIGURE 3. (*a*) Loop-closing event at the free end of a chain hanging under the influence of gravity and harmonically forced horizontally at the attached end. (*b*) The entire length of the chain.

where s is the Lagrangian coordinate along the length. The structural equation (3.3) is solved with an explicit second-order finite difference formulation in space and a fourth-order Runge–Kutta time discretization.

3.2.1. *Validation of the structural solver*

For validation of the structural solver, we consider a chain-like body pinned at one end and swinging under the influence of gravity. The problem of harmonically forcing a hanging chain horizontally at its attached end was used to compare simulations obtained using our method to experiments and numerical studies by Howell & Triantafyllou (1993) and Gobat, Grosenbaugh & Triantafyllou (2002). The success of the comparison was gauged by its success in capturing an initial loop-closing event observed experimentally.

Figure 3 shows the present simulation result with the body closing on itself at $t = 3.38$ s. The simulation was performed for $N = 101$ grid points in order to demonstrate the results of the structural solver for the number of grid points typically used in the fluid–structure calculations. The plot showing the entire length of chain displays the very small scale of the loop. Such tight loop closing is far beyond the expected requirements of the coupled fluid–structure solver (Connell & Yue 2007).

3.3. *Principal parameters*

We define the power coefficient C_P as

$$C_P = \frac{P}{\frac{1}{2}\rho S U^3} \tag{3.6}$$

and the average thrust force, F, is non-dimensionalized as follows, to provide the thrust coefficient:

$$C_T = \frac{F}{\frac{1}{2}\rho S U^2}, \tag{3.7}$$

where ρ denotes the fluid density, S denotes the area of the foil and U the x component of the velocity.

https://doi.org/10.1017/S0022112010006373 Published online by Cambridge University Press

The propulsive efficiency η is defined to be the ratio of useful power over input power, so that

$$\eta = C_T / C_P. \tag{3.8}$$

Using a momentum balance around the flapping foil that neglects the fluctuating quantities and variation in pressure terms, and assuming a uniform flow upstream velocity profile, results in an estimation of the force in the streamwise direction of the aerofoil of

$$C_T = \frac{2}{C} \int_{-\infty}^{\infty} \frac{U}{U_\infty} \left(\frac{U}{U_\infty} - 1 \right) \mathrm{d}y. \tag{3.9}$$

This integral represents a statement of conservation of momentum and has been used extensively to evaluate the mean thrust coefficient on oscillating foils; see Koochesfahani (1989) and Anderson *et al.* (1998).

The drag force acting on the membrane and the power needed for it to be propelled are directly relevant to this study. The total drag force on the wavy foil consists of a friction drag and a form drag due to pressure distribution. Considering an element of the surface along the upper side of the plate $\mathrm{d}s = [\mathrm{d}x^2 + \mathrm{d}y^2]^{1/2}$, its tangential direction is $t = (-\mathrm{d}x, \mathrm{d}y)/\mathrm{d}s$ and the wall-normal direction is $n = (\mathrm{d}y, \mathrm{d}x)/\mathrm{d}s$. The total force per unit length f can be expressed as

$$f_x = f_x^f + f_x^p \, f_y = f_y^f + f_y^p, \tag{3.10}$$

where (f_x^f, f_y^f) is the friction force per unit length and (f_x^p, f_y^p) is the pressure force per unit length.

The total power P_T required for the propulsive motion of the membrane consists of two parts. One is the swimming power P_S, required to produce the lateral oscillation of the flexible plate, and is defined as

$$P_S = - \oint \left(f_x \frac{\mathrm{d}x}{\mathrm{d}t} + f_y \frac{\mathrm{d}y}{\mathrm{d}t} \right) \mathrm{d}s, \tag{3.11}$$

where $\oint$ denotes integration along the membrane surface. The other is the power needed to overcome the drag force, and is represented as P_D:

$$P_D = U \oint (f_x) \, \mathrm{d}s. \tag{3.12}$$

Thus, the total power is $P_T = P_S + P_D$.

The Strouhal number is defined as

$$St = \frac{fA}{U}, \tag{3.13}$$

where A denotes the characteristic width of the jet flow created. Since this is unknown before calculations are made, A is taken to be equal to the total excursion (peak to peak) of the trailing edge of the membrane. The parameter St could also be referred to as the reduced frequency, in analogy with bluff-body wake studies. Here we follow the nomenclature of Triantafyllou *et al.* (1991), because the jet flow generated behind oscillating foils is convectively unstable, hence there is no mode competition between a natural mode and an imposed frequency, and St serves to underline the importance of this number to the instability properties of the jet flow (Triantafyllou *et al.* 1993) and hence to the vortical patterns formed (Anderson *et al.* 1998).

The principal parameters in this problem, in addition to the bending rigidity and structural mass coefficient of the membrane, are

https://doi.org/10.1017/S0022112010006373 Published online by Cambridge University Press

(i) the maximum pitching angle at the leading edge α_{max} and
(ii) the pitching frequency f.

4. Results

We use the coupled fluid/structure numerical model to investigate the fully nonlinear coupled dynamics of the pitching flexible membrane. Our goal is to understand the behaviour of the pitching membrane dynamics and its dependence on the relevant non-dimensional parameters. Our regime of interest is in the limit of high bending rigidity (as close as possible to the fully stiff plate), where the elastic deformation of the membrane may result in an increase of the thrust efficiency.

Simulations are initiated with the body straight and at an angle of attack of 1°. The initial flow condition is of a steady uniform flow. As the simulation starts, the leading edge pitches harmonically, with the angle of attack increasing linearly to the maximum angle of attack inside the first two cycles. Around 10 cycles are needed for both structural and fluid flow periodic steady states to be achieved.

We performed three distinct analyses, by varying one parameter while keeping the remaining two constant:

(i) $EI =$ constant, $\rho_s h =$ constant and varying the maximum leading-edge angle α_{max}.
(ii) $EI =$ constant, $\alpha_{max} =$ constant and varying the structural mass coefficient $\rho_s h$.
(iii) $\rho_s h =$ constant, $\alpha_{max} =$ constant and varying the bending rigidity EI.

4.1. *Maximum leading-edge angle* α_{max}

By varying the one degree of freedom of the system under analysis, for a given rigidity and mass coefficient, we can quantify the structural response to the linear increase in pitching amplitude. For the case of $EI = 1 \times 10^{-5}$ and $\rho_s h = 0.01$, we present in figures 4–6 the results from a series of simulations through a range of maximum leading-edge angles α_{max} and two pitching frequencies f. For each angle, we present four plots, namely the membrane shape at 0.1 Hz intervals for two cycles after steady state is achieved; a time history of the 2-D tail position for ten cycles; vorticity contours of the pitching membrane wake for the fully developed flow and the temporal evolution of the thrust coefficient C_T.

For $\alpha_{max} = 6°$ (figure 4), and looking at both the membrane shape and the cross-stream tail position, we can see that the structural evolution is marked by a pronounced bending around one-half of the chord, which causes a delay for which the tail position reaches its peak. The corresponding vortex wake exhibits an alternating vortex pattern. The alternating vortices are formed at the trailing edge of the membrane, and released close to the maximum tail position for each half-cycle. This alternating vortex wake is responsible for inducing thrust, as can be verified by the temporal evolution of the thrust coefficient C_T plot in figure 4(*d*). As α_{max} increases, the structural response is essentially the same, but obviously with a larger amplitude. For $\alpha_{max} = 8°$ (figure 5), and looking at the temporal evolution of the thrust coefficient C_T plot in figure 5(*d*), we can see that the transient thrust coefficient reaches peaks that increase with increasing α_{max}.

Figure 6 shows the four plots for $\alpha_{max} = 6°$ and $f = 2\,\text{Hz}$. When comparing these results with those for the same value of α_{max} but $f = 1\,\text{Hz}$ (figure 4), we note a noticeable difference in the membrane structural response, with the marked bending occurring closer to the trailing edge. This causes a smaller tail excursion and consequently smaller values for the peak transient thrust coefficient.

https://doi.org/10.1017/S0022112010006373 Published online by Cambridge University Press

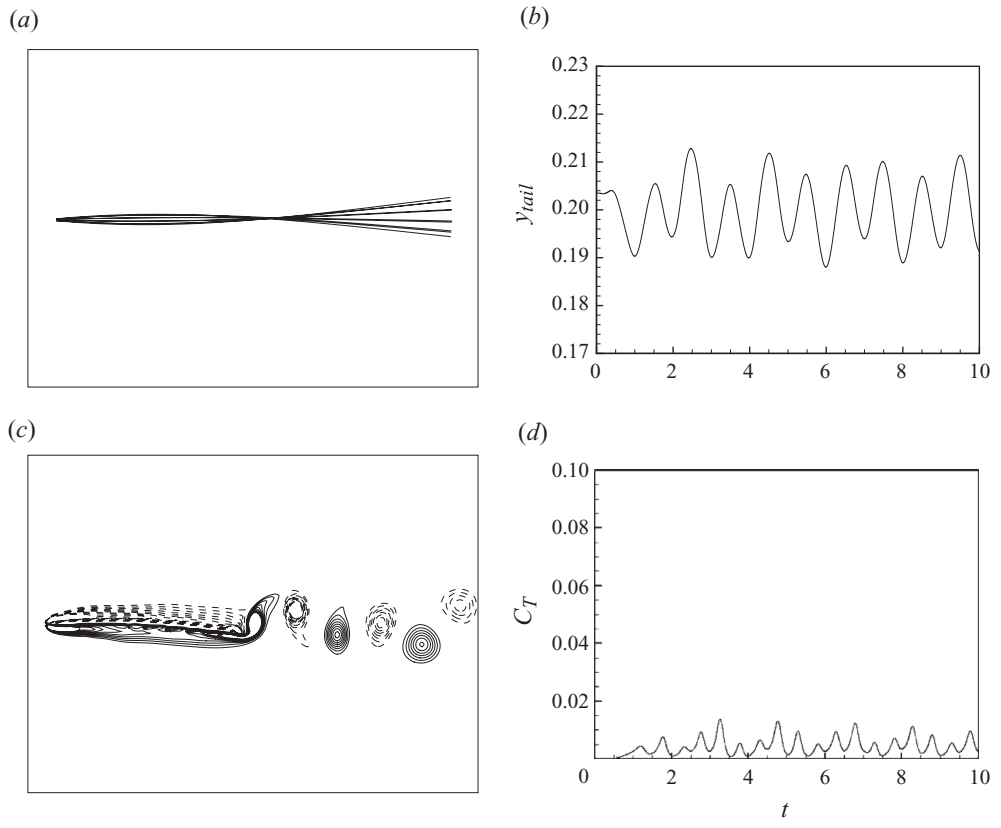

FIGURE 4. (*a*) Membrane shape, (*b*) tail position, (*c*) vorticity field and (*d*) thrust coefficient. Here $EI = 1 \times 10^{-5}$, $\rho_s h = 0.01$ and $\alpha_{max} = 6^\circ$; $f = 1$ Hz.

In figure 7, the averaged results for one cycle of the fully developed flow are presented for the case of $EI = 1 \times 10^{-5}$ and $\rho_s h = 0.01$. Four different plots shown are tail amplitude evolution with α_{max}, tail amplitude evolution with St, thrust coefficient C_T and power C_P with St and efficiency η with St. Tail amplitude remains roughly the same with increased pitching frequency, which means that both thrust and power requirements go up as well as frequency increases. For the same α_{max}, efficiency is higher for the higher-frequency case. As expected, the thrust coefficient increases for increased α_{max}, but with this increase comes the cost of increased power requirements. As such, efficiency decreases with increasing α_{max}.

For the case of $EI = 2 \times 10^{-5}$ and $\rho_s h = 0.01$, we present in figure 8 the results for the simulation with $\alpha_{max} = 6^\circ$ and $f = 1$ Hz. Once again, four plots are presented: the membrane shape at 0.1 Hz intervals for the first 10 cycles, a time history of the two-dimensional tail position for 10 cycles, vorticity contours of the pitching membrane wake for the fully developed flow and the temporal evolution of the thrust coefficient C_T. Looking at both the membrane shape and the cross-stream tail position, we can see that as we increased the bending rigidity, the structural evolution is markedly different from the similar case for $EI = 1 \times 10^{-5}$ (figure 4). For double the bending rigidity, the membrane bends closer to the leading edge, which increases significantly the tail amplitude. The corresponding vortex wake is a more intense alternating vortex pattern, since the generation of the wake vortices is dependent on the

https://doi.org/10.1017/S0022112010006373 Published online by Cambridge University Press

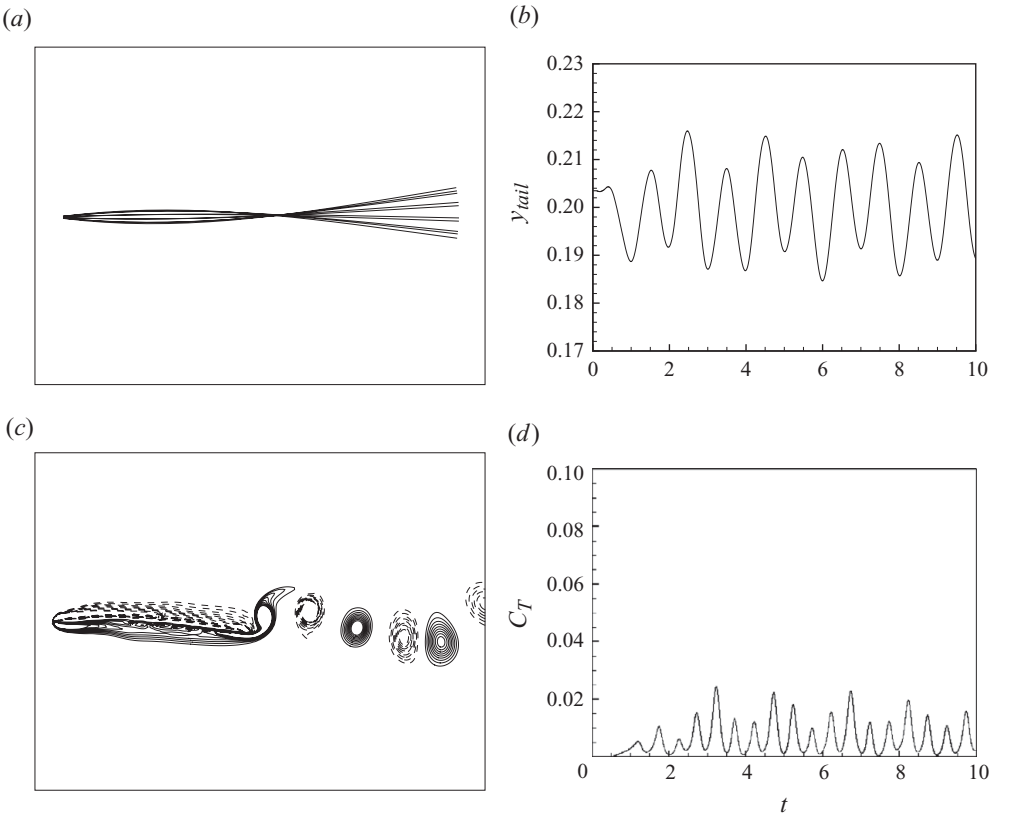

FIGURE 5. (*a*) Membrane shape, (*b*) tail position, (*c*) vorticity field and (*d*) thrust coefficient. Here $EI = 1 \times 10^{-5}$, $\rho_s h = 0.01$ and $\alpha_{max} = 8^\circ$; $f = 1$ Hz.

excursion of the tail. This strong vortex wake is responsible for inducing much more thrust, when compared with the results for the same $\alpha_{max} = 6^\circ$ and half the bending rigidity.

In figure 9, the averaged results for one cycle of the fully developed flow are presented for the case of $EI = 2 \times 10^{-5}$ and $\rho_s h = 0.01$. Again, four plots are shown: tail amplitude evolution with α_{max}, tail amplitude evolution with St, thrust coefficient C_T and power C_P with St and efficiency with St. For this set of results, efficiency η is higher for the largest pitching angle $\alpha_{max} = 8^\circ$. For $\alpha_{max} > 4^\circ$, efficiency markedly grows for increasing values of α_{max}.

4.2. *Structural mass coefficient* $\rho_s h$

The influence of the structural mass coefficient needs to be included if we want to quantify the effect that different density materials and membrane thickness have on the thrust performance of the pitching system. In this study, we varied the structural mass coefficient between 0.01 and 0.04. For the case of $EI = 1 \times 10^{-5}$ and $\alpha_{max} = 8^\circ$, we present in figures 10 and 11 the results from a series of simulations through a range of structural mass coefficients $\rho_s h$.

Figure 10 shows the membrane shape at 0.1 Hz intervals for two cycles of the fully developed flow, as well as the vorticity contours of the pitching membrane wake for the fully developed flow. When comparing the membrane shape for increasing $\rho_s h$, we

https://doi.org/10.1017/S0022112010006373 Published online by Cambridge University Press

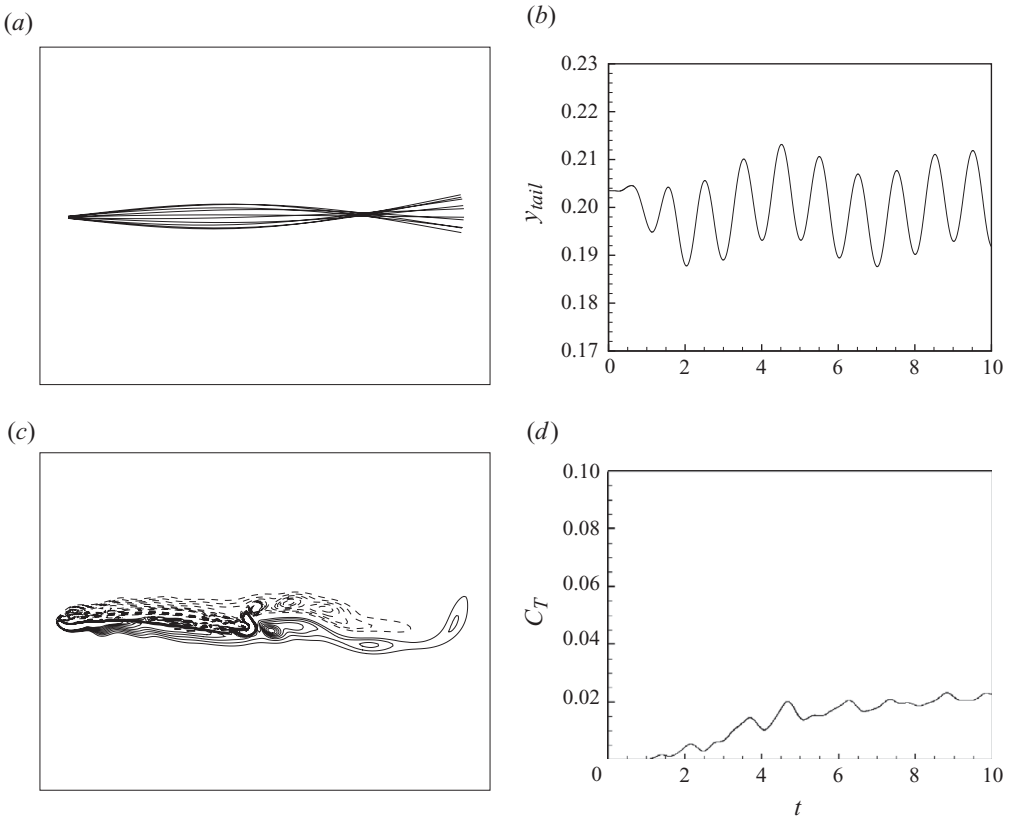

FIGURE 6. (*a*) Membrane shape, (*b*) tail position, (*c*) vorticity field and (*d*) thrust coefficient. Here $EI = 1 \times 10^{-5}$, $\rho_s h = 0.01$ and $\alpha_{max} = 6^\circ$; $f = 2\,\mathrm{Hz}$.

realize that, even if the bending rigidity EI is the same for these four cases, the results presented in figure 5 are also part of this data set, the membrane bending patterns are certainly different. The effect of increasing the structural mass coefficient $\rho_s h$ appears to be an increasing deformation of the membrane at the half-chord region, with little change in the trailing-edge excursion. This can be verified by examining figure 11(*a*), which compares the time history of the trailing-edge position for two cycles. Obviously, this means that the average thrust coefficient will be very similar for $0.02 \leqslant \rho_s h \leqslant 0.04$ (see figure 11*b*).

In figure 12, the averaged results for one cycle of the fully developed flow are presented for the case of $EI = 1 \times 10^{-5}$ and $\alpha_{max} = 8^\circ$. The four plots shown are tail amplitude evolution with $\rho_s h$, St with $\rho_s h$, thrust coefficient C_T and power coefficient C_P with St and efficiency with St. The effect of the structural mass coefficient on efficiency does not have a definite trend, since the trailing-edge amplitude Δy_{tail} has a minimum for c and the values for Δy_{tail} are virtually the same for $\rho_s h = 0.02$ and $\rho_s h = 0.04$. Therefore, efficiency plateaus for $\rho_s h$ higher than or equal to 0.03.

4.3. *Bending rigidity EI*

For given mass ratio $\rho_s h$, forcing frequency f and forcing amplitude α_{max}, the variation of the rigidity of the flexible membrane causes important changes in the

https://doi.org/10.1017/S0022112010006373 Published online by Cambridge University Press

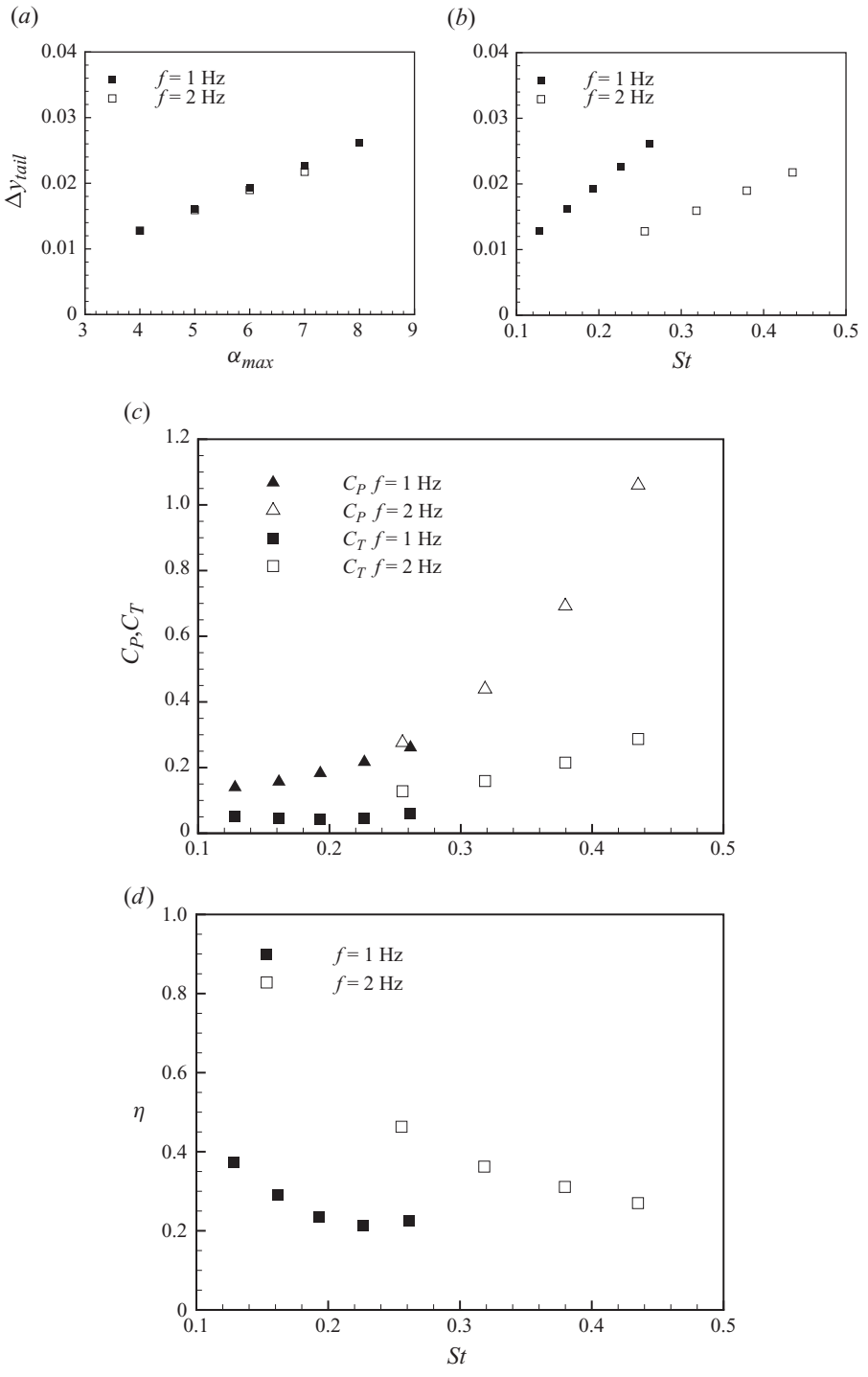

FIGURE 7. Effect of the maximum leading-edge angle α_{max} for two pitching frequencies, with constant bending rigidity $EI = 1 \times 10^{-5}$. (*a, b*) Tail amplitude, (*c*) thrust and power coefficients and (*d*) efficiency; $\rho_s h = 0.01$.

https://doi.org/10.1017/S0022112010006373 Published online by Cambridge University Press

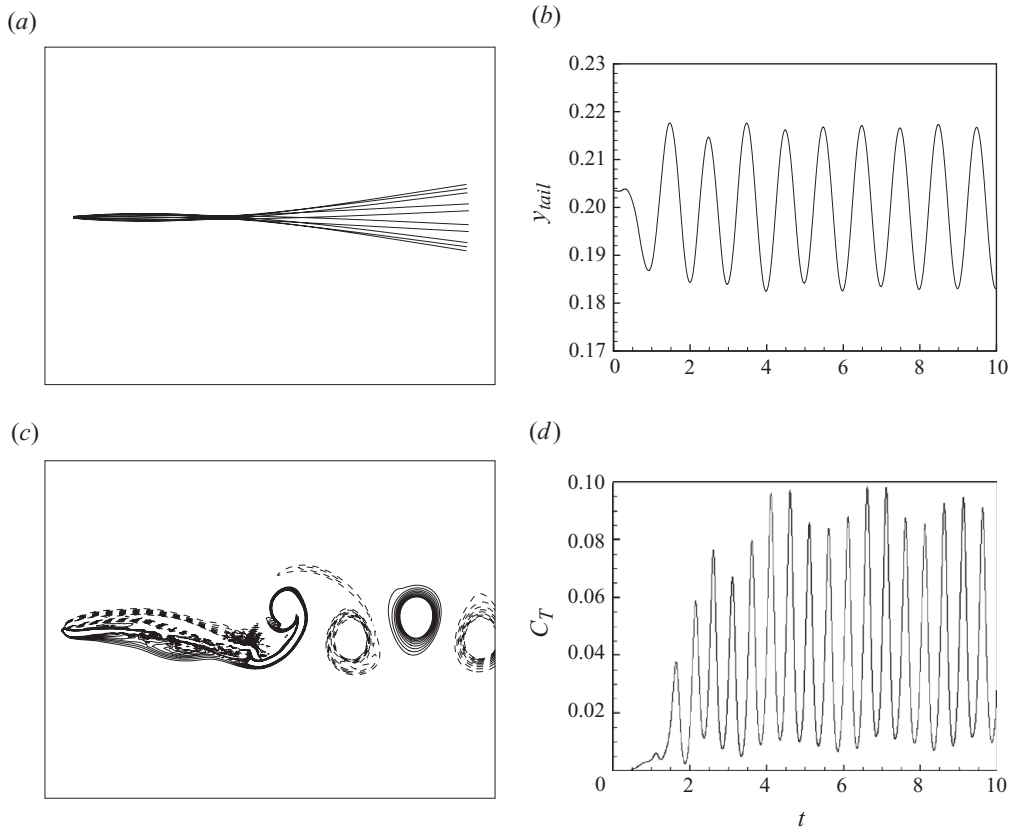

FIGURE 8. (*a*) Membrane shape, (*b*) tail position, (*c*) vorticity field and (*d*) thrust coefficient. Here $EI = 2 \times 10^{-5}$, $\rho_s h = 0.01$ and $\alpha_{max} = 6^\circ$; $f = 1$ Hz.

thrust and power input. As rigidity increases, the wake behind the pitching membrane also undergoes important modifications. Figures 13 and 14 present the results for varying bending stiffness EI, for the cases with $\rho_s h = 0.01$ and $\alpha_{max} = 8^\circ$.

Figure 13 shows the membrane shape at 0.1 Hz intervals for two cycles of the fully developed flow, as well as the vorticity contours of the pitching membrane wake for the fully developed flow. As the bending rigidity increases, the membrane behaviour is more in line with what we could expect from having increasing stiffness. The wake topology changes as well with increasing bending rigidity. For the stiffest membrane, a strong pattern of alternating sign vortices is shed from the flexible membrane, which considerably increases the thrust produced. As it would be expected, for the same α_{max}, as the bending stiffness increases, so does the tail amplitude (figure 14*a*). This translates into increasing thrust coefficient (figure 14*b*).

In figure 15, the averaged results for one cycle of the fully developed flow are presented for cases with $\alpha_{max} = 8^\circ$. Three data sets are presented for $\rho_s h = 0.01$, 0.02 and 0.03, respectively. The three plots shown are St evolution with EI, thrust coefficient C_T and power coefficient C_P with EI, and efficiency with EI. The effect of bending rigidity on efficiency follows trends similar to those explained above. High efficiencies for the same structural mass coefficient can be achieved for values of EI close to the extremes studied here. However, the cases with higher bending rigidity

https://doi.org/10.1017/S0022112010006373 Published online by Cambridge University Press

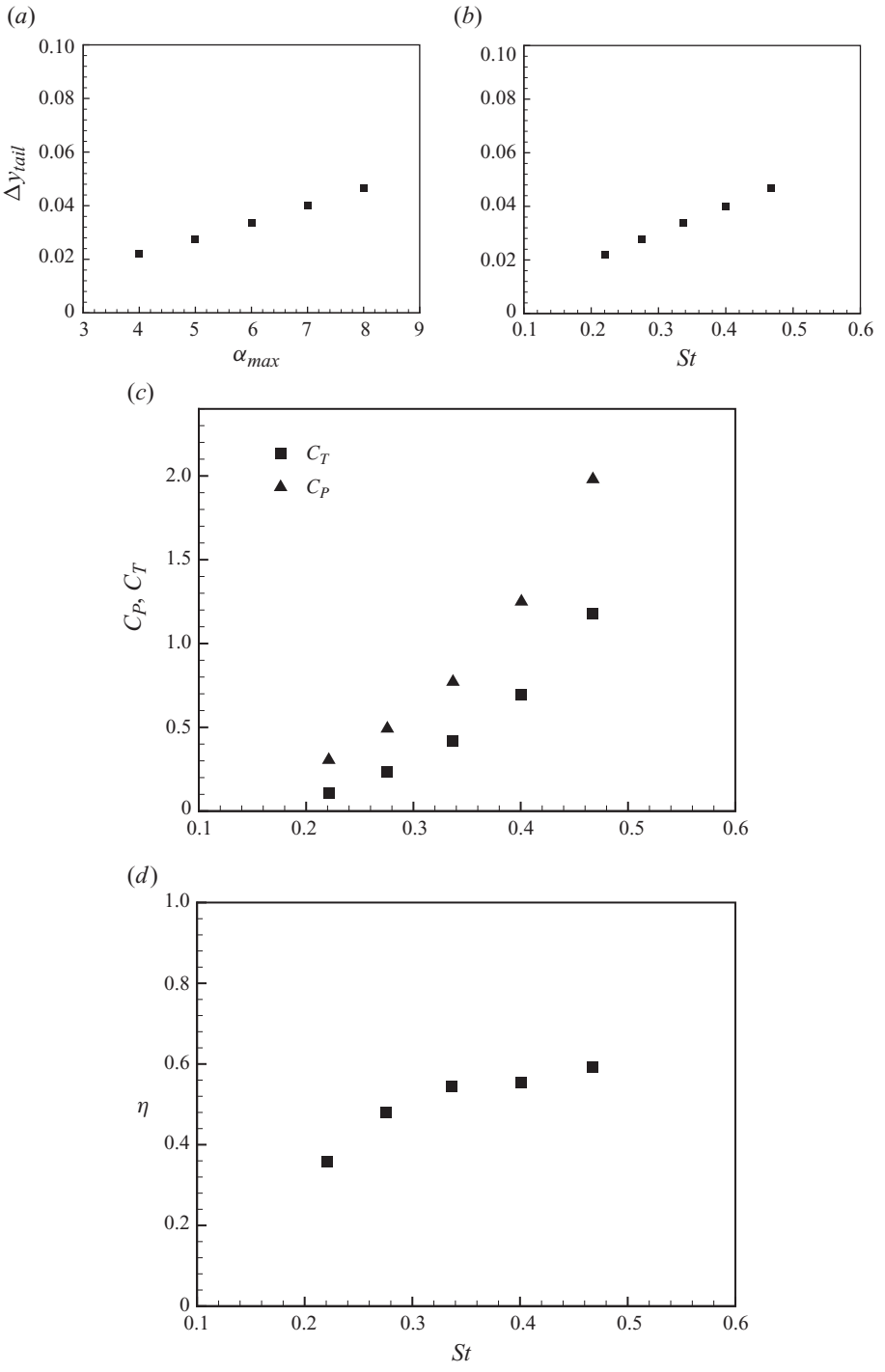

FIGURE 9. Effect of the maximum leading-edge angle α_{max} for pitching frequency $f = 1\,\mathrm{Hz}$, with constant bending rigidity $EI = 2 \times 10^{-5}$. (a, b) Tail amplitude, (c) thrust and power coefficients and (d) efficiency; $\rho_s h = 0.01$.

https://doi.org/10.1017/S0022112010006373 Published online by Cambridge University Press

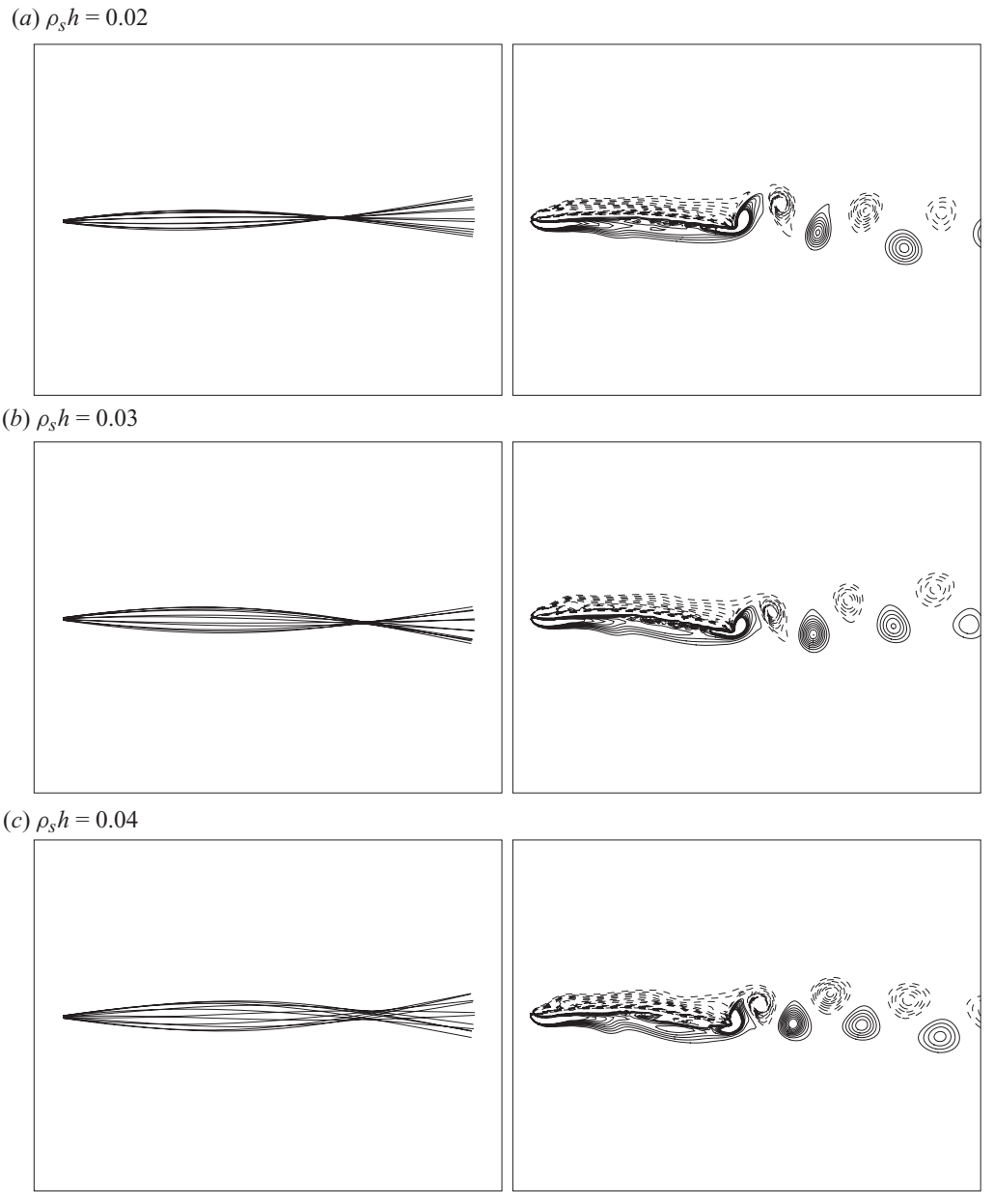

FIGURE 10. (*a–c*) Effect of the structural mass coefficient $\rho_s h$ on membrane shape and vorticity field. $EI = 1 \times 10^{-5}$ and $\alpha_{max} = 8°$; $f = 1$ Hz.

are more suited for propulsion applications, since the thrust coefficients achieved are much higher.

Rigidity has a significant impact on the performance of the propulsive system considered. For a given mass ratio, and in the lower range of mass ratios studied here, forcing amplitude and frequency, the mean thrust and power input both increase as rigidity approaches the higher values; however, the former increases faster and the resulting efficiency increases with increasing rigidity. For higher mass

https://doi.org/10.1017/S0022112010006373 Published online by Cambridge University Press

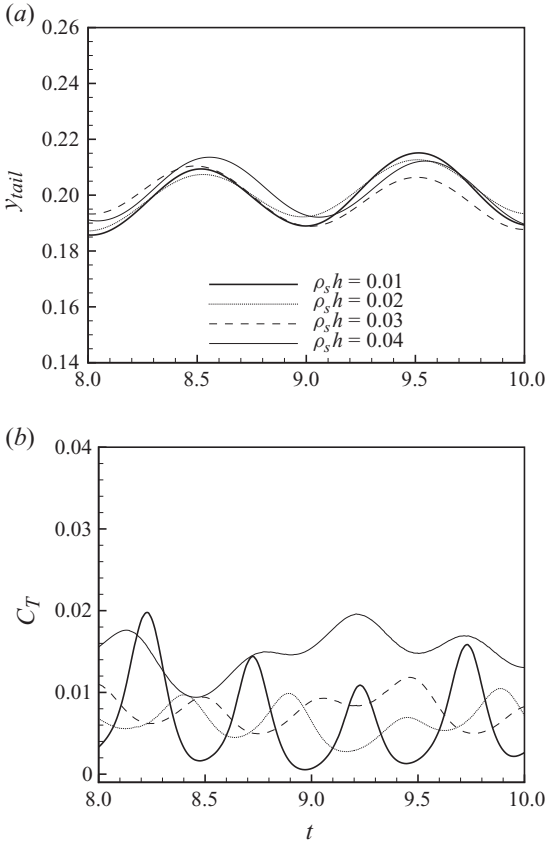

FIGURE 11. Evolution of the (*a*) tail position and (*b*) thrust coefficient for two complete pitching cycles for four different structural mass coefficient $\rho_s h$ values. $EI = 1 \times 10^{-5}$ and $\alpha_{max} = 8°$. $f = 1$ Hz.

ratios, the efficiency drops for higher values of rigidity, as power input increases considerably.

5. Non-dimensional description of membrane behaviour

A simplified description of the motion of the membrane given by (3.3) can be written as

$$\frac{\partial^2 y}{\partial t^2} + \frac{\zeta}{\rho_s h}\frac{\partial y}{\partial t} + \frac{EI}{\rho_s h}\frac{\partial^4 x}{\partial s^4} - T\frac{\partial^2 y}{\partial x^2} = f(x, y), \tag{5.1}$$

where $y(x, t)$ is the displacement of the membrane and the forcing function $f(x, y)$ is the effect of the fluid on the membrane (Allen & Smits 2001). The solution for the displacement of the membrane can be represented as $y(x, t) = \sum_{n=1}^{\infty} \Phi_n(x) A_n(t)$, where $\Phi_n(x)$ represents an orthogonal set of eigenfunctions. Wu (1961) used travelling waves to describe the motion of a swimming plate through water. In Allen & Smits (2001), the choice of the orthogonal basis functions was based on the approximation of the membrane with a pinned Euler–Bernoulli beam and provided a compact,

https://doi.org/10.1017/S0022112010006373 Published online by Cambridge University Press

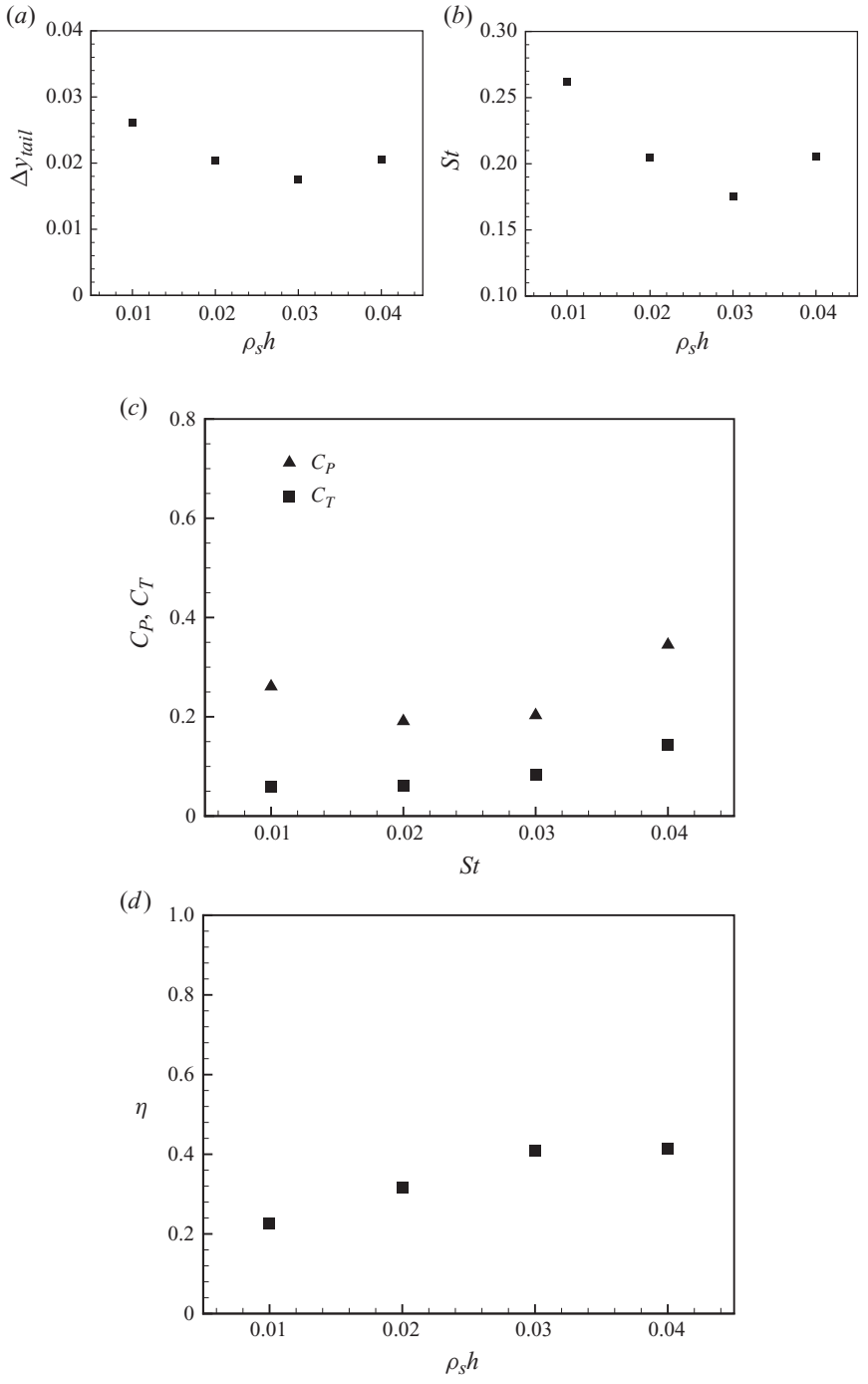

FIGURE 12. Effect of the structural mass coefficient $\rho_s h$ with constant bending rigidity $EI = 1 \times 10^{-5}$. (*a*) Tail amplitude, (*b*) Strouhal number, (*c*) thrust and power coefficients and (*d*) efficiency; $\alpha_{max} = 8^\circ$ and $f = 1$ Hz.

https://doi.org/10.1017/S0022112010006373 Published online by Cambridge University Press

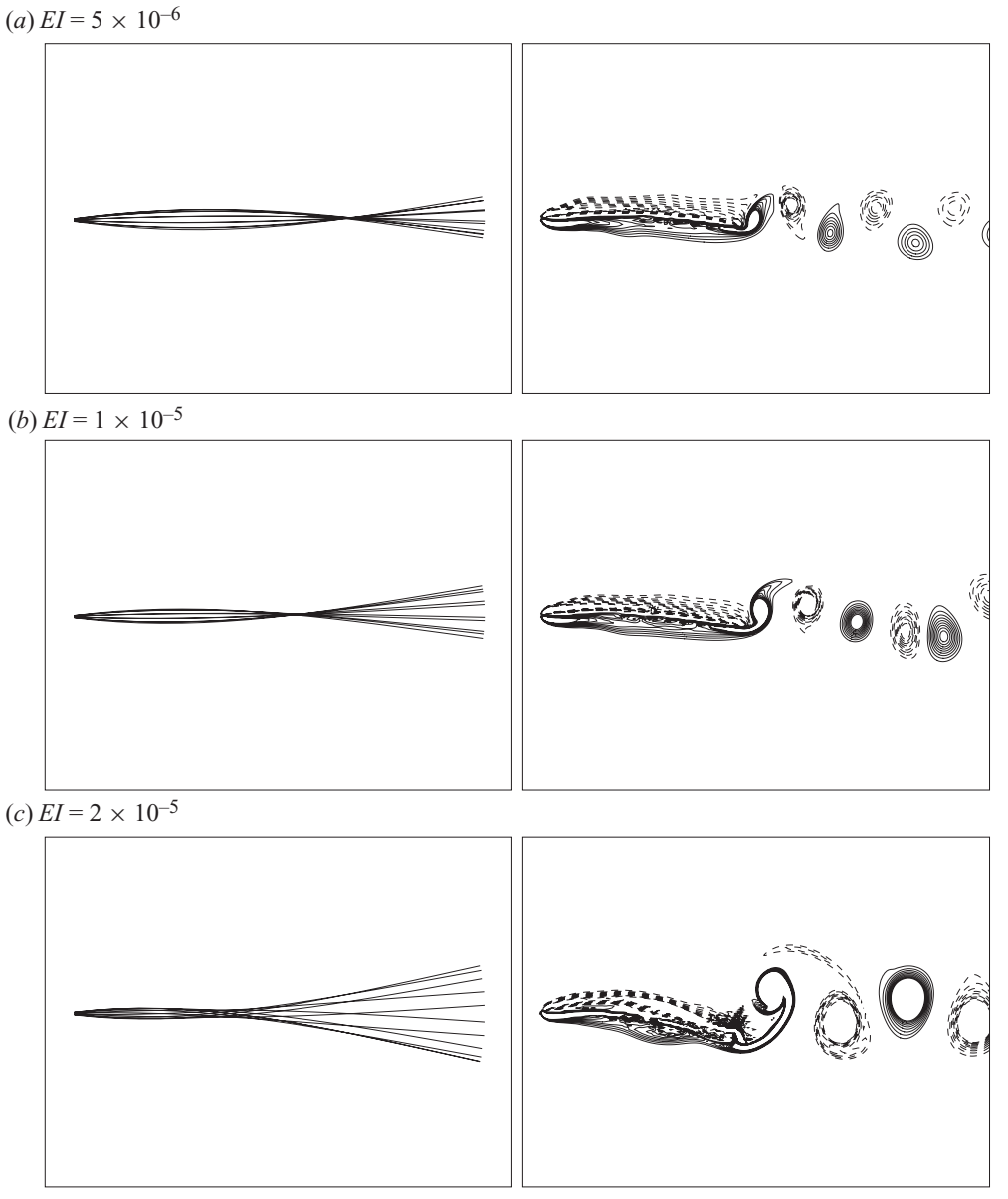

FIGURE 13. (*a–c*) Effect of the bending rigidity EI on membrane shape and vorticity field. Here $\rho_s h = 0.01$, $\alpha_{max} = 8^\circ$ and $f = 1$ Hz.

though not necessarily unique, way to describe the membrane motion. This choice of the orthogonal set of eigenfunctions was the one used in this study.

Neglecting the effects of tension and damping, the Euler–Bernoulli beam equation yields information on the natural frequencies of these modes, which may be expressed as $\omega_n = (\beta_n^2/l^2)\sqrt{EI/\rho_s h}$, where β_n represent the eigenvalues corresponding to $\Phi_n(x)$, which depend on the boundary conditions of the membrane. In this study, the choice of the orthogonal basis functions was based on the approximation of the membrane

https://doi.org/10.1017/S0022112010006373 Published online by Cambridge University Press

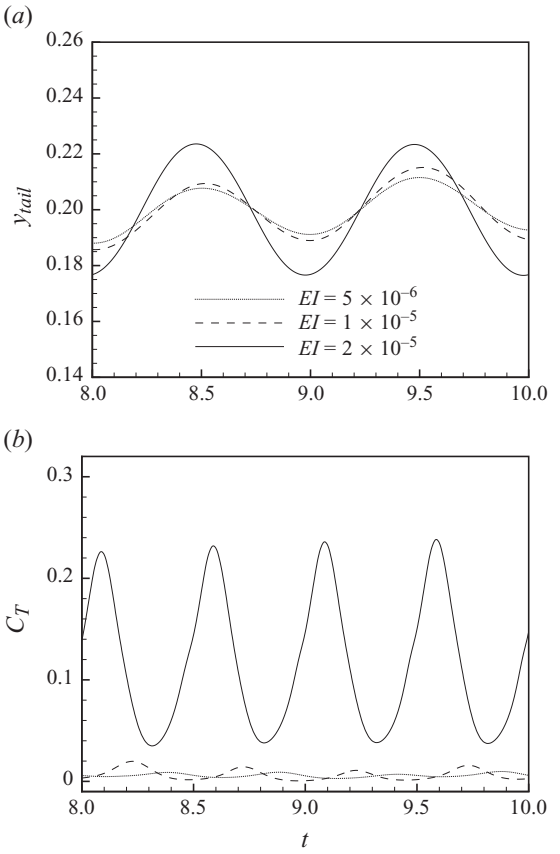

FIGURE 14. Evolution of the (*a*) tail position and (*b*) thrust coefficient for two complete pitching cycles for three different bending rigidity EI values. Here $\rho_s h = 0.01$, $\alpha_{max} = 8^\circ$ and $f = 1$ Hz.

with a clamped Euler–Bernoulli beam, and the modal decomposition was done using the pitching frame of reference.

Data sets for the shape of the flexible membrane have been projected onto the eigenmodes to evaluate the contribution of each mode to the shape of the membrane. Figure 16 shows the relative modal contributions $A_n(t)$, varying in time, for modes 1–4 for the membrane with $EI = 1 \times 10^{-5}$, $\rho_s h = 0.01$ and $\alpha_{max} = 8^\circ$, operating at a frequency of $f = 1$ Hz. The modal contributions start to decay significantly past mode 3 and hence we have a very compact data set to describe the membrane motion. The functions $A_n(t)$ oscillate at the same frequency and display slight phase differences between successive modes. The fact that we have a dominant single mode confirms that the motion of the membrane is a function of the forcing.

The effect of rigidity in the relative modal contributions $A_n(t)$ is shown in figure 17. Two different membranes were calculated, with $\rho_s h = 0.01$, $\alpha_{max} = 8^\circ$ and $EI = 1 \times 10^{-5}$, $EI = 5 \times 10^{-6}$, respectively. The modal contributions start to decay significantly past mode 3, and again we have a very compact data set to describe the membrane motion. As rigidity increases, mode 1 is more dominant and subsequent modes less significant. The effect of decreasing the structural mass coefficient $\rho_s h$, as

https://doi.org/10.1017/S0022112010006373 Published online by Cambridge University Press

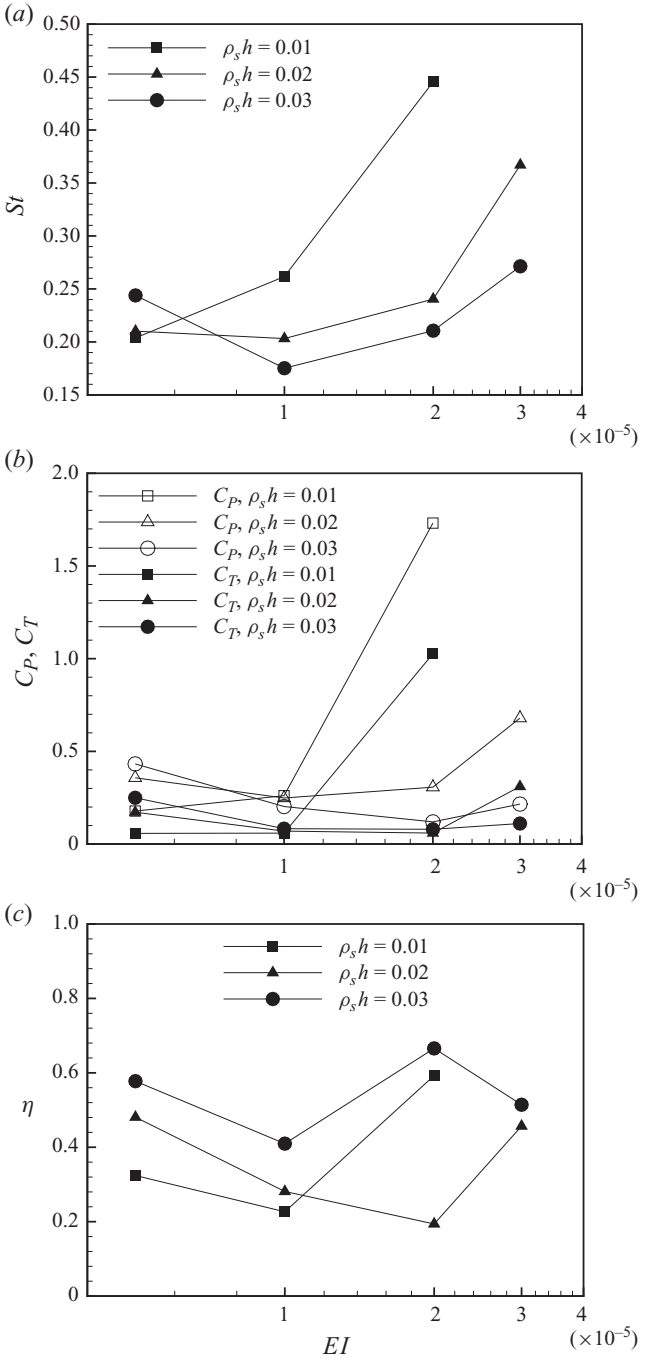

FIGURE 15. Effect of the bending rigidity EI for three different structural mass coefficient $\rho_s h$ values. (*a*) Strouhal number, (*b*) thrust and power coefficients and (*c*) efficiency; $\alpha_{max} = 8°$.

shown in figure 18, is very similar. For increasing values of $\rho_s h$, and maintaining rigidity at $EI = 1 \times 10^{-5}$, mode 1 is slightly less dominant and mode 2 is more dominant.

https://doi.org/10.1017/S0022112010006373 Published online by Cambridge University Press

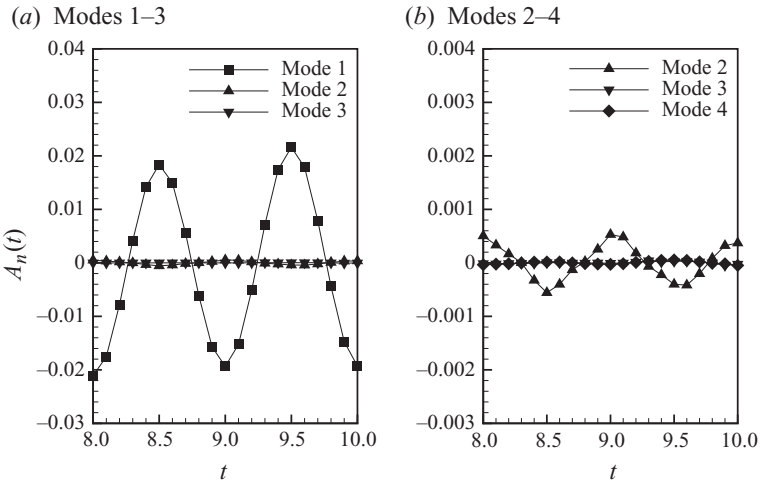

FIGURE 16. Modal contributions to the shape of the membrane. Here $EI = 1 \times 10^{-5}$, $\rho_s h = 0.01$, $\alpha_{max} = 8^\circ$ and $f = 1$ Hz.

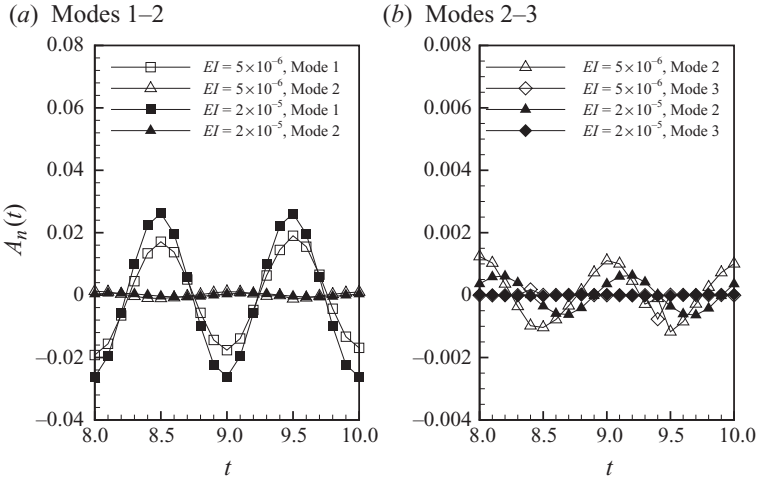

FIGURE 17. Effect of the bending rigidity EI on the modal contributions to the shape of the membrane. Here $\rho_s h = 0.01$, $\alpha_{max} = 8^\circ$ and $f = 1$ Hz.

6. Conclusions

We considered the problem of the pitching motion of a thin flexible body in a uniform flow. For zero extensibility and in the high bending stiffness range, the problem is controlled by the maximum leading-edge angle α_{max}, the bending stiffness EI and to a lesser extent the structural mass coefficient $\rho_s h$.

We developed a direct simulation of the nonlinear coupled fluid–structure problem. Running the fluid/structure fully coupled method, we obtained a systematic set of results for selected values of the bending stiffness and structural mass coefficient, over a broad range of maximum leading-edge angles.

It is shown that the thrust coefficient is primarily a function of Strouhal number, increasing monotonically for increasing St. Efficiency increases for increasing structural mass coefficient and reaches a minimum for intermediate values of the

https://doi.org/10.1017/S0022112010006373 Published online by Cambridge University Press

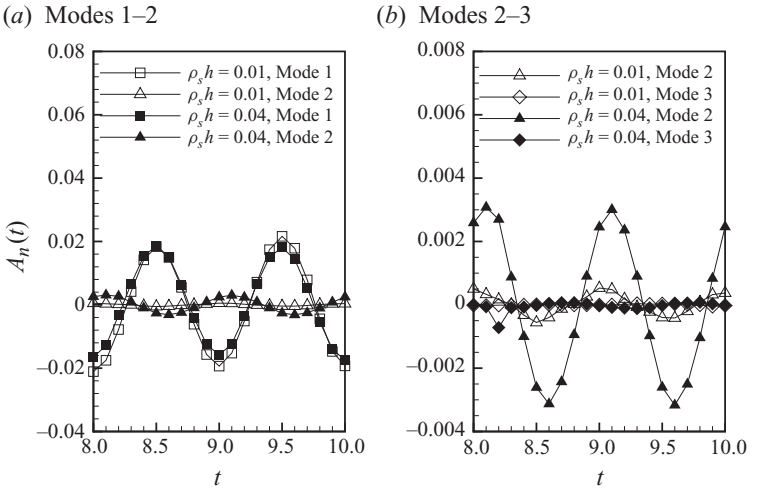

FIGURE 18. Effect of the structural mass coefficient $\rho_s h$ on the modal contributions to the shape of the membrane. Here $EI = 1 \times 10^{-5}$, $\alpha_{max} = 8°$ and $f = 1$ Hz.

bending rigidity. The most interesting aspect of these results is the relatively high values for efficiency that can be obtained for such a simple configuration. Material flexibility increases oscillating plate efficiency, but in contrast, the thrust coefficient for the flexible plate is significantly lower than the results of other researchers. The fact that we obtained high efficiencies for flows produced by a simple flexible membrane suggests that the optimal efficiency condition is somewhat independent of the nature of the thrust-producing device, and more related to the wake topology. Using a simplified description of the oscillating system as an Euler–Bernoulli beam, it is shown that a very compact data set accurately describes the shape of the membrane.

The first author acknowledges the contribution of J. Vennes and the support of FCT (SFRH/BPD/21778/2005 and SFRH/BPD/48160/2008). This work was supported by Air Force Office of Scientific Research. *In memoriam* James J. Allen (1967–2008).

REFERENCES

ALLEN, J. J. & SMITS, A. J. 2001 Energy harvesting eel. *J. Fluids Struct.* **15**, 629–640.

ANDERSON, J. M. & CHABRA, N. 2002 Maneuvering and stability performance of a robotic tuna. *Integr. Compar. Biol.* **42**, 118–126.

ANDERSON, J. M., STREITLIEN, K., BARRETT, D. S. & TRIANTAFYLLOU, M. S. 1998 Oscillating foils of high propulsive efficiency. *J. Fluid Mech.* **360**, 41–72.

BANDYOPADHYAY, P. R. 2005 Trends in biorobotic autonomous undersea vehicles. *IEEE J. Ocean. Engng* **30**, 109–139.

BANDYOPADHYAY, P. R., CASTANO, J. M., RICE, J. Q., PHILIPS, R. B., NEDDERMAN, W. H. & MACY, W. K. 1997 Low-speed maneuvering hydrodynamics of fish and small underwater vehicles. *Trans. ASME: J. Fluids Engng* **119**, 136–119.

BUCHHOLZ, J. H. & SMITS, A. J. 2006 On the evolution of the wake structure produced by a low-aspect-ratio pitching panel. *J. Fluid Mech.* **546**, 433–443.

BUCHHOLZ, J. H. & SMITS, A. J. 2008 The wake structure and thrust performance of a rigid low-aspect-ratio pitching panel. *J. Fluid Mech.* **603**, 331–365.

CONNELL, B. S. H. & YUE, D. K. P. 2007 Flapping dynamics of a flag in a uniform stream. *J. Fluid Mech.* **581**, 33–67.

https://doi.org/10.1017/S0022112010006373 Published online by Cambridge University Press

Dickinson, M. H. & Götz, K. G. 1993 Unsteady aerodynamic performance of model wings at low Reynolds numbers. *J. Expl Biol.* **174**, 45–65.

Fadlun, E. A., Verzicco, R., Orlandi, P. & Mohd-Yusof, J. 1993 Combined immersed-boundary finite-difference methods for three-dimensional complex flow simulations. *J. Comput. Phys.* **161**, 35–60.

Ferreira de Sousa, P. J. S. A, Pereira, J. C. F. & Allen, J. J. 2009 Two-dimensional compact finite difference immersed boundary method. *Intl J. Numer. Meth. Fluids* **65**, 609–624.

Gobat, J. I., Grosenbaugh, M. A. & Triantafyllou, M. S. 2002 Generalized-α time-integration solutions for hanging chain dynamics. *J. Engng Mech.* **128**, 677–687.

Gray, J. 1933 Studies in animal locomotion. I. The movement of fish with special reference to the eel. *J. Expl Biol.* **10**, 88–104.

Howell, C. T. & Triantafyllou, M. S. 1993 Stable and unstable nonlinear resonant response of hanging chains: theory and experiment. *Proc. R. Soc. Lond.* A **440**, 345–364.

Jiménez, J. M., Buchholz, J. H. J., Staples, A. E., Allen, J. J. & Smits, A. J. 2003 Flapping membranes for thrust production. In *IUTAM Symp. on Integrated Modeling of Fully Coupled Fluid–Structure Interactions Using Analysis, Computations, and Experiments, Rutgers University, New Brunswick, NJ* (ed. H. Benaroya & T. Wei), pp. 115–24. Kluwer.

Koochesfahani, M. M. 1989 Vortical patterns in the wake of an oscillating airfoil. *AIAA J.* **27**, 1200–1205.

Liao, J. C., Beal, D. N., Lauder, G. V. & Triantafyllou, M. S. 2003 Fish exploiting vortices decrease muscle activity. *Science* **302**, 1566–1569.

Lighthill, M. J. 1970 Aquatic animal propulsion of high hydromechanical efficiency. *J. Fluid Mech.* **44**, 265–301.

Lighthill, M. J. 1975 *Mathematical Biofluiddynamics.* SIAM.

Mohd-Yusof, J. 1997 Combined immersed boundaries/B-splines methods for simulations of flows in complex geometries. *Center for Turbulence Research, Annual Research Briefs*, pp. 317–327.

Prempraneech, P., Hover, F. S. & Traintafyllou, M. S. 2003 The effect of chordwise flexibility on the thrust and efficiency of a flapping foil. In *Proc. 13th Intl Symp. Unmanned Untethered Submersible Technology (UUST)*, Durham, NH.

Roache, P. J. 1998 Verification of codes and calculations. *AIAA J.* **36**, 696–702.

Schnipper, T., Andersen, A. & Bohr, T. 1970 Vortex wakes of a flapping foil. *J. Fluid Mech.* **633**, 411–423.

Tornberg, A.-K. & Engquist, B. 1991 Numerical approximations of singular source terms in differential equations *J. Comput. Phys.* **200**, 462–488.

Triantafyllou, G. S., Triantafyllou, M. S. & Grosenbaugh, M. A. 1993 Optimal thrust development in oscillating foils with application to fish propulsion. *J. Fluids Struct.* **7**, 205–224.

Triantafyllou, M. S., Hover, F. S., Techet, A. H. & Yue, D. K. P. 2005 Review of hydrodynamic scaling laws in aquatic locomotion and fishlike swimming. *Appl. Mech. Rev.* **58**, 226–237.

Triantafyllou, M. S., Techet, A. H. & Hover, F. S. 2004 Review of experimental work in biomimetic foils. *IEEE J. Ocean. Engng* **29**, 585–594.

Triantafyllou, M. S., Triantafyllou, G. S. & Gopalkrishnan, R. 1991 Wake mechanics for thrust generation in oscillating foils. *Phys. Fluids* **12**, 2835–2837.

Triantafyllou, M. S., Triantafyllou, G. S. & Yue, D. K. P. 2000 Hydrodynamics of fish-like swimming. *Annu. Rev. Fluid Mech.* **32**, 33–53.

Wu, T. Y. 1961 Swimming of a waving plate. *J. Fluid Mech.* **10**, 321–344.

Wu, T. Y. 1971 Hydromechanics of swimming propulsion. Part 1. Swimming of a two dimensional flexible plate at variable forward speeds in an inviscid fluid. *J. Fluid Mech.* **46**, 337–355.

Wu, T. Y. 1975 *Swimming and Flying in Nature.* Reinhold.

Zhang, N. & Zheng, Z. C. 2007 An improved direct-forcing immersed-boundary method for finite difference applications *J. Comput. Phys.* **221**, 250–268.

Zhu, L. & Peskin, C. S. 2002 Simulation of flapping flexible filament in a flowing soap film by the immersed boundary method. *J. Comput. Phys.* **179**, 452–468.

https://doi.org/10.1017/S0022112010006373 Published online by Cambridge University Press